A dynamically equivalent atomistic electrochemical paradigm for the larger-scale experiments ⊘

Asghar Aryanfar ✉ iD ; Trina Dhara; Sunando DasGupta iD ; William A. Goddard, III iD

Check for updates

View Online   Export Citation

Articles You May Be Interested In

Capillary filling dynamics in closed-end carbon nanotubes—Defying the classical Lucas–Washburn paradigm

J. Chem. Phys. (November 2024)

Real-time control of dendritic propagation in rechargeable batteries using adaptive pulse relaxation

J. Chem. Phys. (May 2021)

Effect of the metallicity on the capacitance of gold–aqueous sodium chloride interfaces

J. Chem. Phys. (July 2021)

A dynamically equivalent atomistic electrochemical paradigm for the larger-scale experiments

View Online   Export Citation   CrossMark

Asghar Aryanfar,[1,a)] (iD) Trina Dhara,[2] Sunando DasGupta,[2] (iD) and William A. Goddard III[3] (iD)

AFFILIATIONS

[1] Boğaziçi University, Bebek, Istanbul 34342, Türkiye
[2] Indian Institute of Technology Kharagpur, West Bengal 721302, India
[3] California Institute of Technology, E California Blvd., Pasadena, California 91125, USA

[a)]Author to whom correspondence should be addressed: aryanfar@caltech.edu

ABSTRACT

Electrochemical systems possess a considerable part of modern technologies, such as the operation of rechargeable batteries and the fabrication of electronic components, which are explored both experimentally and computationally. The largest gap between the experimental observations and atomic-level simulations is their orders-of-magnitude scale difference. While the largest computationally affordable scale of the atomic-level computations is ~ns and ~nm, the smallest reachable scale in the typical experiments, using very high-precision devices, is ~s and ~μm. In order to close this gap and correlate the studies in the two scales, we establish an equivalent simulation setup for the given general experiment, which excludes the microstructure effects (i.e., solid–electrolyte interface), using the coarse-grained framework. The developed equivalent paradigm constitutes the adjusted values for the equivalent length scale (i.e., l_{EQ}), diffusivity (i.e., D_{EQ}), and voltage (i.e., V_{EQ}). The time scale for the formation and relaxation of the concentration gradients in the vicinity of the electrode matches for both smaller scale (i.e., atomistic) equivalent simulations and the larger scale (i.e., continuum) experiments and could be utilized for exploring the cluster-level inter-ionic events that occur during the extended time periods. The developed model could offer insights for forecasting experiment dynamics and estimating the transition period to the steady-state regime of operation.

I. INTRODUCTION

Electrochemical systems have allured interest in the modern era.[1] As a result, their intrinsic versatility allows delving into a widespread domain ranging from traditional electroplating[2] to nanotechnology[3] and energy storage devices,[4,5] such as rechargeable batteries.[6] With the beginning of the Fourth Industrial Revolution, durable and adaptable finished metals[7] have been demanded from the larger-scale applications of machinery, automobile industry, and aerospace to the smaller-scale applications of jewelry and decoration.[8] In modern applications, electrodeposition plays a central role in the semiconductor industry,[9,10] and sophisticated micro-/nanofabrication techniques are employed to electrodeposit copper interconnects.[11–13]

As an electrochemical phenomenon, electrodeposition has been widely explored[14] and utilized for coating in applications such as corrosion resistance[15] and mechanical stability.[16,17] As a particular example in rechargeable batteries, the uncontrollable dendritic evolution of the electrodeposited crystals may cause short circuit, thermal runaway, and damage to the cell,[18–20] and several fundamental studies have explored their morphology by conventional[21–24] and advanced methods.[25–27]

Most of the developed models have been derived in the larger continuum scale (~μm) and describe the physical properties of the growing front.[28–30] Earlier models have focused on the establishment of the space-charge zone,[31,32] which describes the existence of the true potential difference within a very small anion-free layer near the electrode surface and leaves the bulk electro-neutral. Later studies have focused on diffusion limited aggregation (DLA)[33,34] and analyzed the mechanism for the formation of tree-like structures.[35]

Nonetheless, as a common feature among all experimental and continuum-level modeling investigations, they are unable to focus

below certain micrometers (~μm).[36–38] Hence, comprehending the respective mechanisms from the atomistic point of view, which mainly occurs at the angstrom scale (~Å) below the microscopic range, remains elusive.

Meanwhile, the atomistic models play a notable role in exploring the behavior of the electrochemical interface below the experimental scales. In particular, the kinetic Monte Carlo (KMC)[39–43] and Molecular Dynamics (MD) simulations[44,45] have shed light on the mechanisms of development of growing structures and metal stripping.[46,47] In this regard, the role of temperature has been addressed[48] and the mechanistic origins of the lithium filaments have been predicted.[49] However, crossing beyond certain nanometers (~nm) and beyond few lattices is computationally unaffordable. Hence, the reach of atomistic simulations will not match the experimentally observable and measurable spectrum, and the remaining gap is in few orders of magnitude. Therefore, the question whether the experimental events can be directly mapped with the simulation results in parallel remains unanswered. The answer could be the design of a miniaturized space that performs in a similar fashion as that of the experimental situation following the physics associated with it.

In order to utilize the larger-scale (~μm) experiments and the smaller-scale atomistic simulation (~nm) concurrently, in this paper, we have established an equivalent simulation paradigm in the smaller scale for the given electrochemical experiment of the larger scale, by adjusting the effective parameters for the diffusion (i.e., D_{EQ}), electromigration (i.e., V_{EQ}), and the determined simulation domain scale (i.e., l_{EQ}). Such equivalency is attained by equating transition dynamics for both the formation and relaxation of the deterministic electrochemical layers. The obtained simulation framework could particularly be useful for investigating inter-atomic events during the transition.

II. METHODOLOGY

The typical scales of atomistic simulations are, in fact, far smaller than those of experiments, both in time (~ns vs ~s) and in space (~nm vs ~μm – mm), as illustrated in Fig. 1. Therefore, the conventional computational power is unable to explore the experimental range. Hence, in order to compare the dynamics of the simulations with the experiments, there could be an equivalent simulation space where the reduced system behaves similar to the larger scale domain. In order to develop an equivalent simulation paradigm that is comparable with the experiments, one needs to scale down the effective experimental values. In this regard, the deterministic factors in the electrochemical dynamics are diffusion and electromigration, neglecting external effects such as convection, and while the former is controlled by the diffusivity D, the latter is ruled by the applied voltage V (i.e., assuming the potentiostatic condition). Hence, we explore the transient electrochemical event, which consists of the formation and relaxation of the concentration gradients during the turn on/off of the voltage/current via adjusting the effective parameters, which include the equivalent domain scale l_{EQ}, the equivalent diffusivity D_{EQ}, and the equivalent applied voltage V_{EQ}.

The generic formation/relaxation dynamics could be obtained by solving the triple non-linear equations for the cationic C_c, the anionic C_a, and the voltage V,[28,31] and during the steady-state
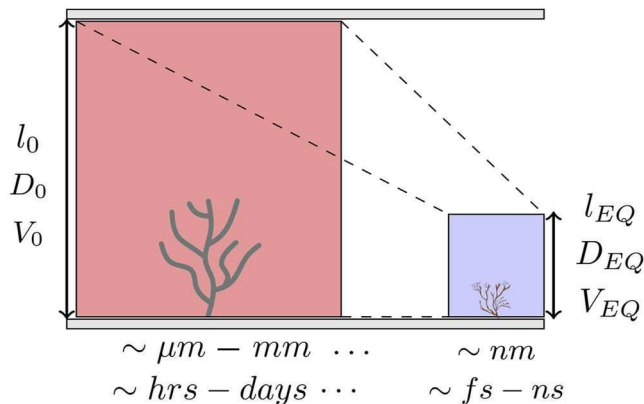

FIG. 1. Comparison between the larger experimental scale on the left with the scale l_0, diffusivity D_0, and performing voltage V_0, with a smaller simulation scale on the right with respective equivalent values of l_{EQ}, D_{EQ}, V_{EQ}.

condition, the entire electrochemical domain forms two distinct regions of gradient and constant zones. The nature of the gradient zone spans from predominantly electrical (i.e., smaller) to physical (i.e., larger) and is illustrated in Fig. 2. Several propositions have been made each layer, which are listed in Table I with their respective typical scales. From the atomistic perspective, the smallest formed layer is the Helmholtz layer (IHP, OHP),[50] composed of the inner and outer compartments that are formed by the attraction of charge carriers to the surface, followed by the diffuse charge region, which was introduced by the Gouy–Chapman model for dilute solutions (<0.001M).[54] Later on, the Stern-layer λ_D was established by combining both of them,[55,56] which was extended by converting the Debye–Hückel theory from a point charge to a flat electrode surface configuration. Larger scale boundary layers (such as space charge x_I) could also form by means of mass transport, where the wave of deficiency of the concentration could travel inside the cell domain. However, if the given time for their establishment/destruction is not sufficient (i.e., such as pulse electrolysis) to converge the bulk value, they will form double diffusion layers (δ_P, δ_s), where one is most sensitive to the applied voltage (i.e., electromigration), while the other is more steady and narrating the mass transfer effect (i.e., diffusion).[53,57] The underlying reason is that the dynamics of the smaller electrical layers (~ atomistic) occurs faster than that of the larger physical layers (~ continuum) as

$$\left(\frac{\partial C}{\partial t}\right)_{\text{Atomistic}} \gg \left(\frac{\partial C}{\partial t}\right)_{\text{Continuum}} \Rightarrow \tau_{\text{Atomistic}} \ll \tau_{\text{Continuum}}, \quad (1)$$

where $\tau_{\text{Atomistic}}$ and $\tau_{\text{Continuum}}$ are the characteristic times in the atomic and continuum scales, respectively. Thus, by the time the concentration boundary layer is formed, the electrical double layers (EDLs) are already in place, and during the transition in the larger scale to the steady state regime, the smaller scale transition has already concluded.

A. Equivalent number of ions N_{EQ}

Ideally, the equivalent simulation paradigm for the given experiment could have identical segregation (i.e., spatial density) of the
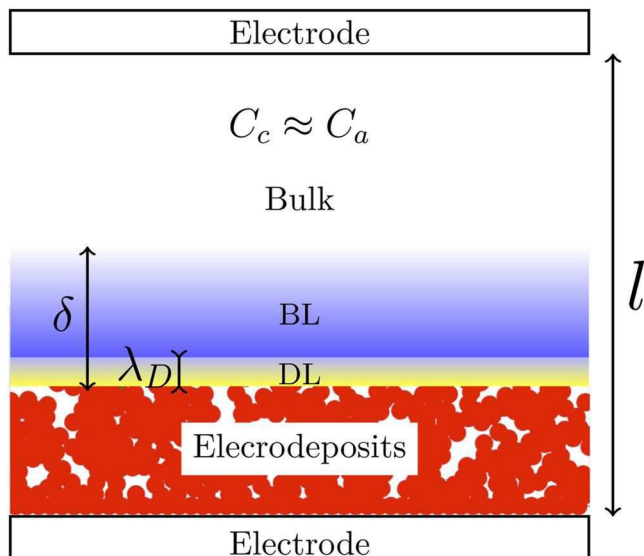
FIG. 2. Electrochemical layers formed during operation. *BL*: boundary layer, *DL*: double layer, δ: diffusion layer, λ_D: Debye length, *l*: cell scale, and C_c, C_a: cationic and anionic concentrations. The continuum-level length and time scales are in the range of $\sim\mu$m – mm and $\sim$hrs – days, respectively, and the atomic-level counterparts are in $\sim$nm and $\sim$fs– $\sim$ns, respectively.

TABLE I. Electrochemical scales.

Name	Acronym	References	Scale (m)	Type
Inn. Helmholtz	*IHP*	50	$\sim 10^{-10}$	
Out. Helmholtz	*OHP*	51	$\sim 10^{-10}$	Atomistic
Debye length	λ_D	52	$\sim 10^{-9}$	
$\vdots$	$\vdots$	$\vdots$	$\vdots$	$\vdots$
Space-charge	x_I	31	$\sim 10^{-6} m$	
Inn. bound.	δ_p	53	$\sim 10^{-5} m$	Continuum
Out. bound.	δ_s	53	$\sim 10^{-4} m$	
Cell scale	l_0	39	$\sim 10^{-3} m$	

ions. Hence, for the three-dimensional experiments of the scale l_0 containing n moles (leading to an experimental concentration of $C_0 = \frac{n}{l_0^3}$) and the two-dimensional equivalent simulations of the scale l_{EQ} with N_{EQ} number of ions, the respective relationship by dimensional analysis would be:

$$N_{EQ} \sim l_{EQ}^2 \left(\frac{nN_A}{l_0^3} \right)^{\frac{2}{3}}, \qquad (2)$$

where N_A is the Avogadro's constant. ($N_A = 6 \times 10^{23} \frac{\text{atom}}{\text{mole}}$). In fact, the above equation ensures similar concentrations between experiments and simulations (i.e., $C_0 \approx C_{EQ}$), which is the measure of their inter-ionic gap.
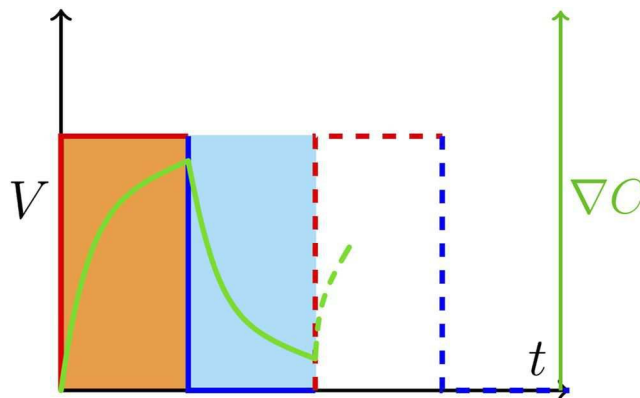

FIG. 3. Formation/relaxation of the concentration gradient ∇C (i.e., green) upon imposing the pulse/rest voltage V (i.e., orange/cyan).

B. Equivalent scale l_{EQ}

Upon applying the voltage/current (potentiostatic/galvanostatic), the electrolytic ions are driven toward the electrode surface. In this regard, if the rate of the reduction reaction (i.e., consumption out) is higher than the supply rate (i.e., diffusion in), it leads to a charge deficiency and forms a concentration gradient (Fig. 3).

The steady-state form of the concentration profile depends on the applied voltage V_0 and diffusivity D_0 of the medium. For a low-enough diffusivity ($D_0\downarrow$) and high-enough applied potential ($V_0\uparrow$), the concentration wave can penetrate into the entire domain l_0 (i.e., continuum). In contrast, for a high-enough diffusivity value ($D_0\uparrow$) and low-enough applied potential ($V_0\downarrow$), the concentration profile remains merely intact and converges to the ambient value in a very thin layer (i.e., atomic scale) in the vicinity of the electrode. Hence, the effective length scale l_{EQ} of the simulation domain could be assigned in between the smaller zone of variation in the voltage V and the larger zone of variation in the concentration C.

Based on the proposed scales for the layers in Table I, an intermediate candidate could be selected as the space-charge zone, where the voltage profile in the vicinity of the electrode surface is expressed as[31]

$$V = V_0 + \Delta V \left(1 - \left(1 - \frac{x}{x_I} \right)^{\frac{3}{2}} \right), \qquad (3)$$

where V_0 is the electrode voltage, ΔV is the inter-electrode potential difference, x is the distance from the electrode surface, and x_I is the thickness of the space charge region obtained as[31]

$$x_I = \left(\frac{9\epsilon\epsilon_0 l_0 V_0^2}{16 k_B T C_0} \frac{z_c z_a}{z_c + z_a} \right)^{\frac{1}{3}}, \qquad (4)$$

where ϵ and ϵ_0 are the relative permittivity of the electrolyte and vacuum permittivity, respectively; l_0 is the inter-electrode gap; V_0 is the
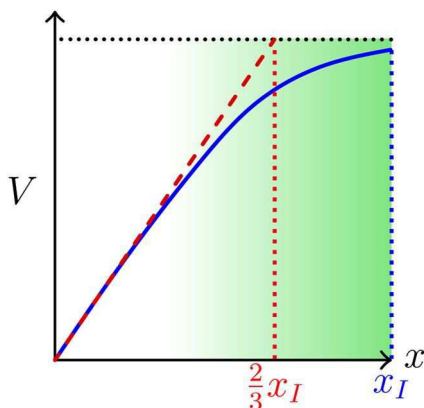
FIG. 4. Approximation for the effective scale of variation in the electric potential in the presence of the applied voltage V. The color intensity is proportional to the ionic concentration.

applied potential; k_B and T are the Boltzmann constant and the temperature, respectively; C_0 is the concentration of the electrolyte; and z_c and z_a are the valence number of the anions and cations, respectively. The electric field E on the surface of the electrode can be obtained as

$$E \sim \frac{\partial V}{\partial x}\Big|_{x=0} = \frac{\Delta V}{\frac{2}{3}x_I}, \tag{5}$$

which signifies the effective length of $\frac{2}{3}x_I$ for the entire voltage difference of ΔV and is visualized in Fig. 4.

Regarding the largest possible scale, the concentration profile could be extended to the entire cell l_0 in the case of fast depletion and lower diffusion. Hence, the range of variations for the equivalent scale l_{EQ} is expressed as

$$\frac{2}{3}x_I \le l_{EQ} \le l_0. \tag{6}$$

Having such a large range to choose from, the space-charge region has been selected in this study as the smallest effective scale in the continuum scale, which contains a confluence of the variations in both voltage V and concentration C,

$$l_{EQ} :\sim x_I, \tag{7}$$

and the voltage across the equivalent experiments and the equivalent scheme remains similar, as

$$V_{EQ} :\sim V_0. \tag{8}$$

C. Equivalent diffusivity D_{EQ}

The transition time scale for the medium of diffusivity D and scale l is in the order of $\sim\frac{l^2}{D}$. Hence, in order to match the dynamics

of the scales, the diffusivity D_{EQ} in the equivalent scheme has been scaled down proportionally as

$$D_{EQ} :\sim \left(\frac{l_{EQ}}{l_0}\right)^2 D_0, \tag{9}$$

which leads to $D_{EQ} \ll D_0$ and ensures that for a computationally affordable equivalent simulation time interval δt_{EQ}, a considerable number of the ions remain inside the simulation domain and only part of them exit the boundary, which are treated by means of a periodic boundary condition.

D. Equivalent time segmentation δt_{EQ}

Regarding the time segmentation δt_{EQ}, one could break down the displacements of the ions further into diffusion (i.e., D) and electromigration terms (i.e., $\mathbf{E}$). In this regard, the coarse scale model in time has been exploited, where the electrochemical movement of the ions is the cooperative sum of the diffusion-driven and electromigration-driven displacements.

Diffusion-wise, the ions tend to collide and repel each other during the random walks (i.e., Brownian motion) at a given coarse time interval δt, and the diffusional front progress $\delta\mathbf{r}_D$ would be

$$\delta\mathbf{r}_D = \sqrt{2D\delta t}\,\hat{\mathbf{g}}, \tag{10}$$

where D is the diffusivity of the ions in the electrolytic solution and $\hat{\mathbf{g}}$ is a random unit vector, implying the Brownian motion. In fact, the expression $\sqrt{2D\delta t}$ explains the mean square displacement (MSD) of the diffusive front, attained directly by solving the classical diffusion equation.[58]

Regarding the electromigration, the charge carriers exposed to an external electric field $\mathbf{E}$ initially accelerate and quickly reach a constant drift velocity of $\mu\mathbf{E}$. Hence, their electromigration displacement $\delta\mathbf{r}_M$ in the given time interval δt is obtained as

$$\delta\mathbf{r}_M = \mu\mathbf{E}\delta t, \tag{11}$$

where μ is the mobility of the ionic species within the electrolyte. Therefore, the total ionic displacement $\delta\mathbf{r}$ is the sum of the aforementioned factors as shown in the following:

$$\delta\mathbf{r} = \delta\mathbf{r}_D + \delta\mathbf{r}_M. \tag{12}$$

Due to the unidirectional effect of the electric field, the ions will gradually migrate from one electrode side (i.e., V^+) and accumulate in the vicinity of the other (i.e., V^-), while the diffusion tends to uniformize the distribution. The efficacy of the ionic transport depends on the competitiveness of the electromigration term over the diffusion term. As an example, a dense electrolyte ($D\downarrow$) with a high applied voltage ($V\uparrow$) will have a dominant electromigration, while a dilute electrolyte ($D\uparrow$) with a lower applied voltage ($V\downarrow$) will have a significant diffusional effect. Herein, we assume the latter, with the electromigration competitiveness with 10% of the diffusional term. Noting the Einstein correlation of mobility

18 November 2024 17:54:51

and diffusivity $\left(\mu = \frac{D_{EQ}e}{k_B T}\right)$ and the average electric field $\mathbf{E} \approx \frac{V_{EQ}}{l_{EQ}}$, one gets

$$\frac{D_{EQ}e}{k_B T}\frac{V_{EQ}}{l_{EQ}}\delta t_{EQ} >\sim 0.1\sqrt{2D_{EQ}\delta t_{EQ}}, \tag{13}$$

which provides the lower limit for the simulation time segmentation δt_{EQ}. On the other hand, during each movement, a significant fraction of the ions should remain inside the domain and not exit the boundaries frequently $\{\delta \mathbf{r}_D, \delta \mathbf{r}_M\} \sim l_{EQ}$, which means

$$\left\{\sqrt{2D_{EQ}\delta t_{EQ}}, \frac{D_{EQ}e}{k_B T}E\delta t_{EQ}\right\} \sim l_{EQ}, \tag{14}$$

and this provides the upper boundary for the simulation time segmentation δt_{EQ}. Therefore, the range of suitable simulation time is obtained as

$$\sim \frac{0.02}{D_{EQ}}\left(\frac{l_{EQ}}{V_{EQ}}\frac{k_B T}{e}\right)^2 < \delta t_{EQ} <\sim \min\left\{\frac{l_{EQ}^2}{2D_{EQ}}, \frac{l_{EQ}k_B T}{D_{EQ}Ee}\right\}. \tag{15}$$

To summarize, we have redefined the experimental parameters $(l_0, D_0, V_0, C_0, \delta t_0)$ to get the equivalent values $(l_{EQ}, D_{EQ}, V_{EQ}, C_{EQ},$ and $\delta t_{EQ})$ to be used in the equivalent simulation paradigm. The new equivalent paradigm possesses identical chronological behavior for the formation/relaxation of the concentration gradient when the voltage/current is turned on/off.

III. EXPERIMENTAL OBSERVATION

In order to observe the concentration gradient upon applying voltage and discuss the associated details from a morphological perspective, the colorimetric technique has been used, based on Hibbert and Melrose (1989).[59] The experimental design consists of a 5×5 cm^2 Whatman filter paper (grade 1) substrate, fixed inside a plastic chamber, with the electrodes, fixed with a tape. The cathode is a 32 gauge copper wire in the center, with the periphery insulated and the tip in contact with the substrate. The anode is a 28 gauge copper wire bent to a 2 cm diameter ring [Fig. 5(a)]. Initially, the paper substrate was damped with a 1M copper sulfate solution to avoid the evaporation loss of the electrolyte solution. The electrolyte solution was prepared by dissolving 62.4g of copper sulfate pentahydrate (CuSO$_4$.5H$_2$O, EMPLURA, 99%) into 250 ml of deionized water (Milli-Q, 99.8%). As soon as the voltage was applied (KEITHLEY 2410 1100 V source-meter), the deposition started to take place at the cathode cross section. Right after the formation of the microstructure, the paper strip was immersed into 1M sodium hydroxide to solidify the ionic distribution. The paper strip turned greenish blue, which is due to the reaction with the NaOH solution to form copper hydroxide [Cu(OH)$_2$(solid)]. The strip was vacuum-dried for 15 min to eliminate excess water and was observed under an optical microscope (LEICA, DM6000M) [Fig. 5(b)]. Due to the formation of carbonate (dull green) during long exposure to air, the entire process has terminated by 25 min.

Figure 6 shows the sample of the optical observations $(10x)$, where the color transitions from light blue to darker turquoise when moving away from the electrodeposited interface. Upon application of the voltage, the growing front consumes the nearest available ionic
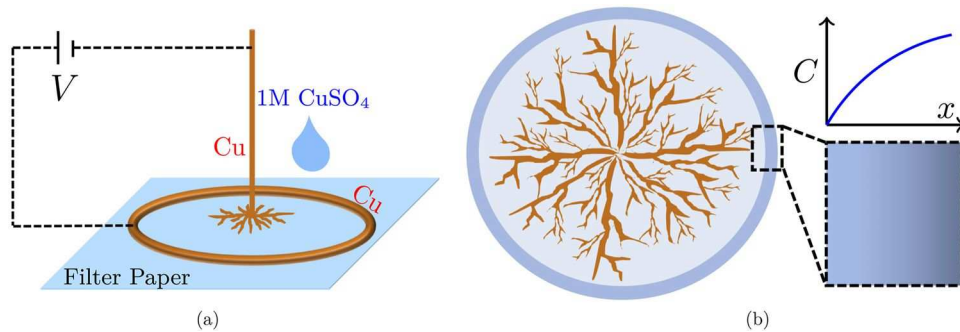
FIG. 5. (a) The experimental setup (side view). The electrochemical cell consists of the copper rod and circular disk electrodes. The electrodeposits evolve on the paper substrate damped with the electrolyte solution (1M CuSO$_4$ in water). (b) The colorimetry of the concentration gradient (top view). Observation of the concentration gradient in the electrodepositing interface, where the light intensity is indicative of the ionic depletion.
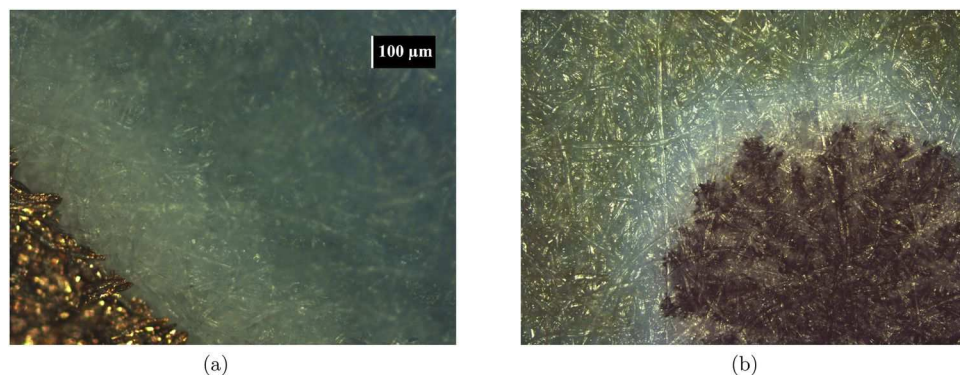
FIG. 6. Observation of the growing electrodeposits on the paper substrate, where a color transition is observed moving from the surface to the bulk. The lighter color on the surface is correlated with the ionic depletion, forming the concentration gradient with respect to the darker color in the bulk. (a) A sample of the flat electrode/electrolyte interface. (b) A sample of the rounded electrode/electrolyte interface.

18 November 2024 17:54:51

species. When the voltage is turned off and the special position of the Cu^{2+} ions is locked by converting them to the solid hydroxide compound, the lack of copper ions near the interface is reflected in terms of the color transition that appears herein. Figure 6(a) shows the flat interface after 8 min upon applying 2 V, while Fig. 6(b) illustrates the curved interface formed after 2 min with a voltage of 3.6 V. The higher light intensity at the interface could be correlated with the absence of the ionic concentration, while the inside bulk region remains darker. The scale of the depletion zone is measured as ~400 μm and ~250 μm in these figures, respectively.
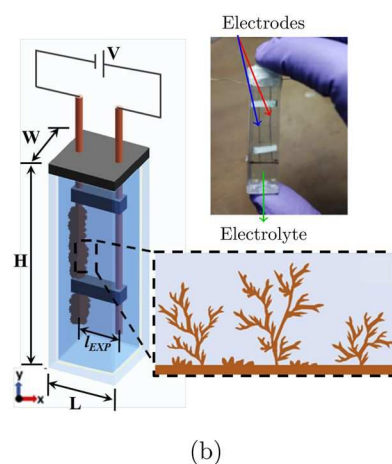
A. Fractal exploration

The electrodeposits could grow in fractal form to a certain extent. The underlying reason in the continuum scale (larger than ~μm) is that the concentration distribution pattern is governed by similar relationships governing the diffusive flux and Gauss relationship (i.e., Laplacian) for their respective voltages. Hence, any higher/lower scale in the continuum realm could grow similar morphologies. However, moving into atomistic (less than ~μm) scales, the Brownian dynamics becomes the main contributor to the movements. The pattern of formation can become more stochastic, although the stochasticity might still form a similar branching pattern to a lesser extent. Therefore, the morphology in the continuum scale might scale down in the fractal form to some extent (as long as it can be called continuum), and in particular, when moving to the atomic scale, it might not replicate the larger-scale geometries.

In order to predict the fractal tendency, we have performed experiments. The experimental setup is shown in Fig. 7(a), where two copper wires were utilized as the electrodes and copper sulfate solution is used as the electrolyte, and the transparent cuvette with the electrodes and electrolyte plays the role of the entire electrochemical cell for real-time visualization of the growing interface, as detailed out in Fig. 7(a). Hence, we have observed the side view of the wire electrode over which the electrodeposits accumulate.

FIG. 8. Example of estimating the fractal dimension d_f based on the box-counting method, where based on the scale of the fitting boxes r, there is a required number of boxes N to cover the entire structure. The slope of the plot of log N vs log r achieves the fractal dimension d_f (in this figure, $d_f \approx 1.9$).

The grown morphology has shown high dependency on the solute concentration C_0, chemical composition, applied voltage V, and the experimental time-span t. As an example, the electrolytic concentration of 1.0M made a denser morphology than its 0.01M counterpart, with a relatively lower propensity for being fractal in the observed scale.[21]

Figure 9 shows four samples of such images, where the first two images are optical observations and the last two images are acquired through observations from the electrode surface using an electron microscope (JEOL, FE-SEM, Model No.: JSM-7800 F).

(a)

(b)

FIG. 7. Experimental observation. (a) Cell and measurement setup.[61] (b) Experimental observation for observing the fractal dimension of the electrodeposits.[24]
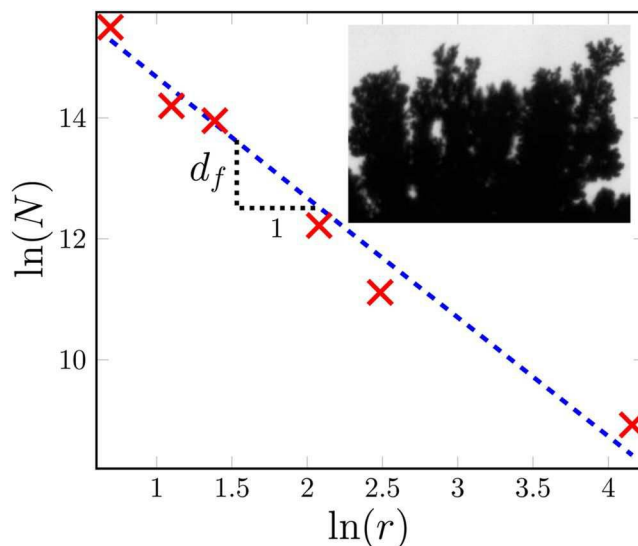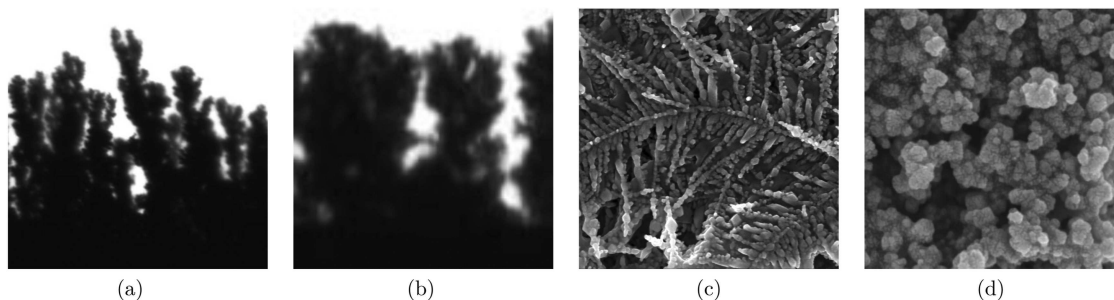
FIG. 9. Exploring the fractal dimension d_f for four different scales. (a) $l \approx 1250$ μm, $d_f \approx 1.42$. (b) $l \approx 420$ μm, $d_f \approx 1.41$. (c) $l \approx 2.2$ μm, $d_f \approx 1.16$. (d) $l \approx 0.8$ μm, $d_f \approx 1.11$.

The captured images are analyzed in the ImageJ software[60] to obtain the value of the fractal dimension by the box counting method.

The fractal dimension d_f can be estimated through the following relationship:[62]

$$N = \epsilon^{-d_f}, \tag{16}$$

where N is the number of measurement units and ϵ is the scaling factor.[63] In fact, the scaling factor ϵ shows how much a part of the fractal shape (i.e., line) is divided to establish a base for the formation of the next-level lower fractal shape. As an example, $\epsilon = \frac{1}{3}$ for the development of the Koch Snowflake.[64] For image processing purposes, the Minkowski–Bouligand dimension has been used as a method for estimating the fractal dimension.[65,66] Such a method works based on box-counting, which relies on the number of boxes N with the box scale r that are required to cover the entire image set.[67] Such box-counting methods have been conceptually proven for estimating the fractal dimension d_f during the radial propagation of the dendritic microstructures by means of diffusion limited aggregation (DLA).[68] Hence, plotting log N (N: the number of required boxes that occupy the structure) vs log (r) (r: box size as a variable), the obtained slope could be interpreted as the fractal dimension d_f, as follows:[69]

$$d_f \approx -\frac{\Delta(\log N)}{\Delta(\log r)}. \tag{17}$$

A sample of estimating the fractal dimension for an image is shown in Fig. 8, where the image is covered with the various box sizes $r = \{2, 3, 4, 8, 12, 64\}$ pixels, the obtained number of boxes to cover the structure is $N = \{10\,378, 4690, 2715, 730, 337, 15\}$, and the estimation for the fractal dimension is $d_f \approx 1.9$.

In addition, the generalized diffusivity D within the medium of fractal wiring, in three dimensions (i.e., surface fractal), has been experimentally approximated as[70]

$$D \approx D_0 d^{d_f - 2}, \tag{18}$$

TABLE II. Estimated fractal dimensions.

Figure	Optical microscopy (~mm)	SEM (~μm)
Fractal dimension d_f	≈ 2.41	≈ 2.08

where D_0 is the diffusion coefficient of the ideal smooth surface in the absence of the fractal microstructure and d is the effective diameter of a diffusing molecule. Noting that exploration of the fractal dimension is only possible for 2D images via the line fractal method, the average fractal dimension for the larger scale optical observation is $d_f \approx 1.41$, and for the smaller scale SEM observations, it is obtained as $d_f \approx 1.08$. In order to project the line fractal computation in 2D images into the surface fractal version in 3D construction, the number 1 is added to the computed fractal dimension. Hence, the realistic estimations for the fractal dimensions d_f of the microstructures shown in Fig. 9 are shown in Table II.[71]

The obtained fractal dimensions from the optical microscopy (~mm) and scanning electron microscopy (SEM; ~μm) scales indicate that while the dividing pattern in the optical scale occurs with the rate of $d_{f,Optical} \approx 1.41$, the dividing pattern for the SEM scale occurs at $d_{f,SEM} \approx 1.08$, which are fairly different by $\approx 31\%$. This suggests that the pattern of fractal dividing does not occur at the same rate across the entire continuum scale and the fractal propensity of the microstructure across the continuum scale seems to be small. In addition, in the atomistic scale (~ Å), the random Brownian motion can develop a certain fractal propensity. While the atoms are colliding-repelling, they might replicate a certain set of collision distances (i.e., mean free path) across different scales frequently. In addition, there are certain common behaviors across the scales at the atomic level, such as the coefficient of restitution when bouncing back from a boundary. These analogous behaviors could generate similar morphologies in those atomic scales and form fractal microstructures.

In addition, one can notice that since the estimated fractal dimensions tend to the 2 ($d_f \rightarrow 2$), based on the relationship in Eq. (18), the fractal tendency is not fairly effective on the diffusivity ($D \approx D_0$), and the diffusivity D remains fairly constant across the continuum scale.

IV. NUMERICAL VERIFICATION

In order to prove the performance of the prescribed small-scale equivalent system, herein we validate its harmony with the experiments. In this regard, the formation/relaxation transition in the concentration gradient of the active ions due to the application/removal of voltage between a larger-scale experiment and the smaller-scale equivalent simulation paradigm has been explored.

18 November 2024 17:54:51

TABLE III. Experimental parameters (left) and the equivalent simulation parameters (right). The electrolyte solution is $1M$ $CuSO_4$ in deionized water.

Experimental (continuum, ~μm)				Simulation (atomistic, ~nm)			
Parameter	Value	Unit	References	Constant	Value	Unit	References
l_0	5	mm	24	l_{EQ}	160	nm	Equation (4)
V_0	71	mV	Measured	V_{EQ}	71	mV	Equation (8)
A	3×10^{-5}	m^2	Designed	N_{EQ}	1.8×10^4	()	Equation (2)
C_0	1000	$mol\,m^{-3}$	Designed	D_{EQ}	2.4×10^{-19}	$m^2 s^{-1}$	Equation (9)
i	42	$A\,m^{-2}$	Applied	nB	24	()	Assigned
D_0	2.3×10^{-10}	$m^2 s^{-1}$	72	δt_0	10	ms	Assumed
				δt_{EQ}	300	s	Equation (15)

TABLE IV. Common constants.

Constant	Value	Unit	References	Constant	Value	Unit	References
e	1.6×10^{-19}	C	77	k_B	1.4×10^{-23}	$J\,K^{-1}$	77
ϵ	78	()	78	T	298	K	77
z_c	2	()	For Cu^{2+}	N_A	6×10^{23}	mol^1	77
z_a	2	()	For SO_4^2	ϵ_0	8.9×10^{-12}	$F\,m^{-1}$	77

The experimental values are given in Table III (left), where the current density i is applied experimentally vs the voltage measured from the earlier setup in an electrochemical cell,[24] and the corresponding simulation values are obtained (right) as follows:

- The scale of the smaller-scale variations has been taken in the order of space-charge region x_I as[31]

$$x_I = \left(\frac{9 \times 78 \times 8.9 \times 10^{-12} \times 5 \times 10^{-3} \times 0.071^2}{16 \times 1.4 \times 10^{-23} \times 298 \times 1000 \times 6 \times 10^{23}} \times \frac{4}{2+2} \right)^{1/3}$$

$$\approx 1.6 \times 10^{-7} \text{ m.} \tag{19}$$

- The number of atoms N_{EQ} was obtained by setting the identical sparsity of the ions [Eq. (2)] as follows:

$$N_{EQ} \approx \left(1000 \times 6 \times 10^{23} \right)^{\frac{2}{3}} \times \left(1.6 \times 10^{-7} \right)^2$$

$$\approx 1.8 \times 10^4 \text{ Atoms.}$$

- The equivalent diffusivity D_{EQ} in smaller scale l_{EQ} is obtained by setting the identical transition times [Eq. (9)] as

$$D_{EQ} \approx \left(\frac{1.6 \times 10^{-7}}{5 \times 10^{-3}} \right)^2 \times 2.3 \times 10^{-10}$$

$$= 2.4 \times 10^{-19} \frac{m^2}{s}.$$

The common constants are given in Table IV.

A. Formation of ∇C

When a voltage is applied, the concentration gradients in both scales start to form due to an abrupt increase in the rate of consumption of the ionic species with a higher outflux compared to the rate of influx of the ions toward the electrode. The continuum and atomistic concentration dynamics have been established using separate methods, as shown below.

1. Continuum (~ μm)

The concentration $C(y,t)$ varies in both time t and space y (distance from the electrode). In the absence of convection, the transition for the cations ($+$) and anions ($-$) is governed by diffusion and migration terms in $1D$ as[31]

$$\begin{cases} \dfrac{\partial C_+}{\partial t} \approx D_+ \dfrac{\partial^2 C_+}{\partial y^2} + z_+ \mu_+ \dfrac{\partial V}{\partial y} \cdot \dfrac{\partial C_+}{\partial y} + z_+ \mu_+ C_+ \dfrac{\partial^2 V}{\partial y^2}, \\ \dfrac{\partial C_-}{\partial t} \approx D_- \dfrac{\partial^2 C_-}{\partial y^2} - z_- \mu_- \dfrac{\partial V}{\partial y} \cdot \dfrac{\partial C_-}{\partial y} - z_- \mu_- C_- \dfrac{\partial^2 V}{\partial y^2}. \end{cases}$$

For our case of binary solution, one has $C = \frac{C_+}{\nu_+} = \frac{C_-}{\nu_-}$,[73] where ν_+ and ν_- are the number of cations and anions per dissociation of one molecule of electrolyte. Multiplying by the right coefficients and summing, one can simplify as follows:

$$\frac{\partial C}{\partial t} = D_0 \frac{\partial^2 C}{\partial y^2}, \tag{20}$$

where $D_0 = \frac{z_+ \mu_+ D_- + z_- \mu_- D_+}{z_+ \mu_+ + z_- \mu_-}$ is the ambipolar diffusivity.[74] In addition, the mobility μ and diffusivity D_0 are related by the Einstein relationship as $\mu = \frac{D_0 q}{k_B T}$, and for our case of copper sulfate $CuSO_4$, $z_+ = z_- = 2$ and $q_+ = q_- = 2e^-$. The ambipolar diffusivity D_0 is simplified into

$$D_0 = \frac{2D_+ D_-}{D_+ + D_-}.$$

The end value of ambipolar diffusivity D_0 is reported from an experimental work in the literature (Ref. 72). Denoting C_i^j as the concentration in the location $y(i)$ and time $t(j)$, we can discretize Eq. (20) as follows:

$$C_i^{j+1} = Q_1 C_i^j + Q_2 \left(C_{i+1}^j + C_{i-1}^j \right), \tag{21}$$

where Q_1 and Q_2 are the quotients obtained as follows:

$$Q_1 = 1 - \frac{2D_0 \delta t}{\delta y^2}, \quad Q_2 = \frac{D_0 \delta t}{\delta y^2}. \tag{22}$$

The updated concentration in every next time step t^{j+1} (i.e., C_i^{j+1}) should contain the same sign as the value in the time t^j (i.e., C_i^j). This gets translated to $Q_1 > 0$ that forms the stability criterion as follows:[75,76]

$$\delta t < \frac{dy^2}{2D_0}, \tag{23}$$

which means that the frequency of the concentration measurements in time should be large-enough to be able to capture the frequency of the concentration variations in space.

The initial condition for the bare solution would be

$$C(0) = C_0, \tag{24}$$

which will reduce upon applying the voltage V since in the electrode zone, the rate of outflow reaction is greater than the rate of inflow transport. For the applied current density of i, the respective ionic flux would be $j = \frac{i}{nF}$, and the boundary conditions would be

$$\frac{\partial C}{\partial x}(0, t) = \frac{\partial C}{\partial x}(l_0, t) = \frac{i}{nFD_0}. \tag{25}$$

As the concentration gradient ∇C increases, the inflow mass transport to the interface becomes more competitive with the outflow from the boundaries, and the concentration profiles arrive at the steady-state condition value C_{SS}. Due to the asymptotic convergence of Eq. (21), the threshold of 99% is assumed to be enough for the convergence to the steady-state value C_{SS} in the electrode surface, as follows:

$$\frac{C_0 - C(0, t)}{2C_0} \approx 99\%, \tag{26}$$

where $C(0, t)$ is the concentration at the electrode/electrolyte interface. The case of full depletion on the electrode surface is considered ($C_{SS} \approx 0$).

2. Atomistic (~ nm)

The equivalent simulations in charging have been run in the square domain of scale l_{EQ} ($0 \leq x, y < l_{EQ}$) with the equivalent number of atoms (N_{EQ}) and the equivalent diffusivity D_{EQ} calculated from Eqs. (2) and (9). In order to measure the concentration profile, we have defined the number of bins nB, which are the spans of a specific length and contain the atoms within. Initially, the free ions N_{EQ} are scattered randomly within the medium, which fairly generates a uniform distribution. Hence, the average number of ions $\bar{N}$ in each bin would simply be

$$\bar{N} = \frac{N_{EQ}}{nB}. \tag{27}$$

Regarding the voltage boundary condition, V_{EQ} in the atomistic scale is obtained from Eq. (8). Since the larger scale experiments were performed galvanostatically for a significantly long period of time (~ hrs), the initial transition period for the buildup of the voltage can be approximated as having negligible effect and the quasi-steady state equivalent of the voltage V_{SS} for the applied current density i_{SS} has been chosen. In other words, during the steady state operation,

$$i_{SS} \propto V_{SS},$$

where the constants i_{SS} and V_{SS} are considered as the boundary conditions of the larger (i.e., continuum) and smaller (i.e., atomistic) scales.

Applying the equivalent voltage V_{EQ} obtained from Eq. (8), the electric field $\mathbf{E}$ is generated in the domain of diffusivity D_{EQ}. Hence,

$$V_{EQ}(l_{EQ}) = V_0.$$

Subsequently, the coarse grained model is run based on Eqs. (10) and (11). In this regard, for the ions reaching the electrode surface, the periodic boundary condition (PBC) is applied, which means that for any reduction reaction (i.e., losing an ion), an oxidation reaction occurs on the counter-electrode (i.e., adding an ion) and ensures charge conservation. The periodic boundary condition PBC has been implemented as follows:

$$\begin{cases} y_i > l_{EQ}, & y_i = \text{rem}\,(y_i, l_{EQ}), \\ y_i < 0, & y_i = l_{EQ} - \text{rem}\,(|y_i|, l_{EQ}), \end{cases} \tag{28}$$

where rem stands for the remainder after dividing to the medium scale l_{EQ}. Similarly, the PBC applies to the horizontal ionic position x_i as well.

Using the simulation values in Table III and simulating the movements for each segmentation δt_{EQ}, the number of atoms in each bin iB varies and is recorded. Due to stochastic variations in the bin values iB, non-linear fitting has been performed to estimate the concentration profile as a linear distribution.

The simulation continues until the 99% convergence criterion as follows:

$$\frac{N_{nB} - N_1}{2\bar{N}} \approx 99\%, \tag{29}$$

which is the atomistic version of convergence for the criterion defined in Eq. (26), assuming full depletion in the steady state condition.

Figure 10(a) illustrates the transient dynamics at the electrode interface from both continuum and atomistic perspectives. In addition, Fig. 10(b) shows the evolution of the concentration profile in these two scales, where the normalized time $\hat{t}$ is the ratio of the specified time during the transition to the convergence time t_c ($\hat{t} = t/t_c$). In addition, the normalized concentration (i.e., $\hat{C} = C/C_0$) and the voltage ($\hat{V} = 1$) are defined.

Hence, to summarize, the governing relationships for the dynamics of the continuum and atomistic scales are given in the following:

$$\begin{cases} \text{Continuum:} & \dfrac{\partial C}{\partial t} = D_0 \dfrac{\partial^2 C}{\partial y^2}, \\ \text{Atomistic:} & \delta \mathbf{r} = \sqrt{2D_{EQ}\delta t_{EQ}}\,\hat{\mathbf{g}} + \dfrac{D_{EQ}e}{k_B T}\mathbf{E}\delta t_{EQ}. \end{cases}$$

During formation and relaxation, while the concentration map for the continuum scale gets updated, the concentration map for the atomic scale is obtained via dividing the space into a finite number of bins, and the number of ions in each bin gets updated in time.

B. Relaxation of ∇C

When the voltage is turned off, the concentration gradients in both scales start to vanish, which is explained separately in the larger and smaller scales in the following.

1. Continuum ($\sim \mu m$)

The relaxation of the concentration profile occurs with the dynamics as described in Sec. IV A 2, except that the initial condition is assumed to be the full depletion at the electrode surface (i.e., 0), which leads to the concentration of $2C_0$ on the other side due to mass balance; hence,

$$C(y,0) = \frac{2C_0}{l}y. \tag{30}$$

The boundary during relaxation is simply the blocking electrode, since there is no voltage V (and current i), and any ionic flux will not exist,

$$\frac{\partial C}{\partial y}(0,t) = \frac{\partial C}{\partial y}(l,t) = 0. \tag{31}$$

The convergence condition has been assumed as the 5% threshold of reverting back to the uniform concentration, as follows:

$$\frac{C_0 - C(0,t)}{2C_0} \approx 5\%. \tag{32}$$

2. Atomistic ($\sim$ nm)

Similarly, the relaxation of the concentration profile in atomistic scale occurs with the same dynamics as shown in Sec. IV A 2, except under the condition below.

The initial condition is assumed to be the full depletion at the electrode surface, which contains the concentration $2\bar{N}$ on the counter-electrode side; hence,

$$N_{iB} = 2\frac{iB}{nB}\bar{N}, \tag{33}$$

where N_{iB} is the number of ions in the bin indexed.

For the boundary condition, the simulation has been performed for the span of $iB = 2, \ldots, nB - 1$ and, since there is no ionic flux in the boundaries, the boundary conditions are simply identical to those of the blocking electrodes, with no concentration gradient, as follows:

$$N_1 := N_2, \quad N_{nB} := N_{nB-1}. \tag{34}$$

For convergence, the ionic movement during relaxation will occur only due to diffusion ($\delta \mathbf{r}_D$), and finally, the convergence criterion is similarly expressed as the 5% threshold of reverting back to the uniform concentration, as follows:

$$\frac{\bar{N} - N_1}{2\bar{N}} \approx 5\%. \tag{35}$$

Figure 11(a) illustrates the temporal relaxation of the concentration gradient in both continuum ($\sim 10^{-3}$m) and atomic ($\sim 10^{-7}$m) scales. In addition, the profile variation of the concentration gradient at various times is shown in Fig. 11(b).

V. RESULTS AND DISCUSSIONS

The very close correlation of the formation in the normalized concentration gradients $\Delta \hat{C}$ [Figs. 10(a) and 11(a)] and its value $\hat{C}$ [Figs. 10(b) and 11(b)] suggests the direct harmony between the larger-scale continuum and smaller-scale atomistic frameworks, which occurs to be in the order of charging time regime for the batteries (i.e., $\sim$h). In this regard, the projection of the profile in the atomistic paradigm is due to the finite number of bins where the ions can randomly move from one bin to another. Such Brownian motion can induce heterogeneity (i.e., sharp variation) in the obtained concentration profile. Conversely, in the continuum paradigm, the very large number of ions (i.e., Avogadro-scale) leads to averaged movements, forming a smoother profile.

While the main drive for the formation of concentration gradients in the experimental (continuum) scale is the current density of the boundary i, the drive in the simulation (atomistic) paradigm is the equivalent voltage-based electric field, which has been measured from the experiments ($V \sim i$). In fact, the mass balance relationship of the ions in the vicinity of the electrode would be

$$Out \sim In - \delta C, \tag{36}$$

where Out is the depletion of the ions from the boundary (current i), In is their supply to the electrode (diffusion), and δC is the respective change in the electrode surface. In fact, initially, the abundance of the ions will make the transition reaction limited as

$$Out \sim -\delta C, \tag{37}$$

while later on, the supply of the ions gradually increases and, in the steady-state condition, becomes comparable with the depletion rate. Hence,

$$Out \sim In. \tag{38}$$

Regarding the transition dynamics toward the steady-state condition, the ions need to be transported from the bulk solution and
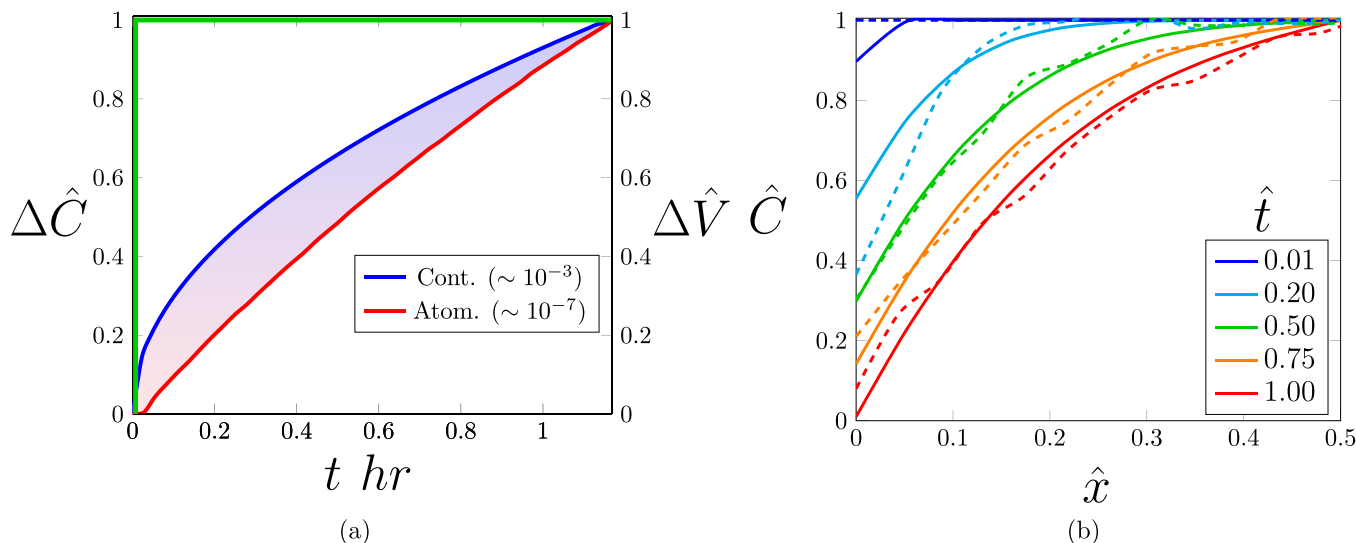
18 November 2024 17:54:51

FIG. 10. Correlation between the continuum and atomistic scales during the formation of concentration gradients. (a) The transient evolution of the concentration gradient in the continuum (blue) as well as in the equivalent simulation (red) scales. (b) The evolution of the concentration profile in the half cell at different time lapses as a fraction of the convergence time in both continuum (solid) and atomistic (dashed) scales.

later deposited on the interface of the reaction sites. Since these two events occur in series, the rate of the electrodeposition will be determined by the event of smaller pace. Hence, the charging (reaction) rate will determine the dominant factor as follows:

$$\begin{cases} \text{Slow charging } (J_{\text{Rxn}} < J_{\text{Diff}}), & \text{reaction limited,} \\ \text{Fast charging } (J_{\text{Rxn}} > J_{\text{Diff}}), & \text{diffusion limited.} \end{cases} \quad (39)$$

An interesting combination of reaction-limited and diffusion-limited formation occurs during the pulse charging, which can be imagined as the periodic application of DC. Therefore, the periodic formation of a concentration gradient, followed by the relaxation process, is expected. The applied pulse period could get short enough such that a smaller-scale transient concentration gradient forms (i.e., reaction-limited), while the larger-scale concentration profile (i.e., diffusion-limited) gets established gradually. Such a dual-diffusion layer has been observed in pulse electrolysis,[53,57] where the applied pulsating frequency oscillates the smaller-scale concentration profile, while the larger-scale counterpart remains fairly intact.

From a broader perspective, the reaction on the electrode during charging is imposed by the applied external voltage ΔV, which is of an electrical nature. On the other hand, its response is the formation of the concentration gradient ΔC, which has a physical nature. While these two events occur concurrently, they differ in the transition time and formation scale, as summarized in Table V.

One can notice that diffusional displacements in both atomistic and continuum frameworks are correlated with $\sqrt{D\delta t}$, and in order to computationally afford such a long time interval, since $D_{EQ} \ll D_0$, one must have $\delta t_{EQ} \gg \delta t_0$. In addition, in order to generate concentration gradient during charging, the electromigration term needs to be competitive with the diffusion term to a certain extent, which has

been taken with 10% efficacy [Eq. (13)]. Taking that efficacy as 10%, Eq. (15) provides the lower limit for the simulation time interval δt_{EQ} as follows:

$$\delta t_{EQ} >\sim \frac{0.02}{D_{EQ}}\left(\frac{l_{EQ}}{V_{EQ}}\frac{k_B T}{e}\right)^2,$$

which turns to be $(\delta t_{EQ} > 287s)$ for the data given in Table III, although in total, the diffusional displacements in the atomistic framework still remain smaller than those in the continuum version,

$$\left(\sqrt{2D\delta t}\right)_{\text{Continuum}} \gg \left(\sqrt{2D\delta t}\right)_{\text{Atomistic}},$$

and the reduction of the diffusivity $(D_0 \rightarrow D_{EQ})$ at the expense of increasing time segmentation $(\delta t_0 \rightarrow \delta t_{EQ})$ gets justified.

Needless to mention, for the particular electrochemical system composed of reactive electrode metals (i.e., lithium Li and sodium Na) and the organic electrolyte, the additional solid electrolyte interface (i.e., SEI) forms at the electrode surface, which is an ionically conducting and mechanically separating porous organic network. Therefore, they could affect the diffusivity D during the last stage of electrodeposition relative to the bulk electrolyte, as the reactant ions must additionally penetrate through the microstructure. Hence, two media with distinguished diffusivities, D_{SEI}[79] and D_{Bulk}, could be considered during the charge transport. The SEI *per se* is composed of the organic (from the electrolyte) and inorganic (from the electrode) compartments.[80–82]

However, for the generalized case of electrode/electrolyte interaction, as in this study (Cu electrode with $CuSO_4$ in water electrolyte), a significantly thinner oxide layer forms the interface via a reaction with the oxygen in the solution. The typical scale of such a layer for copper Cu is ~2 nm,[83] and compared with the common
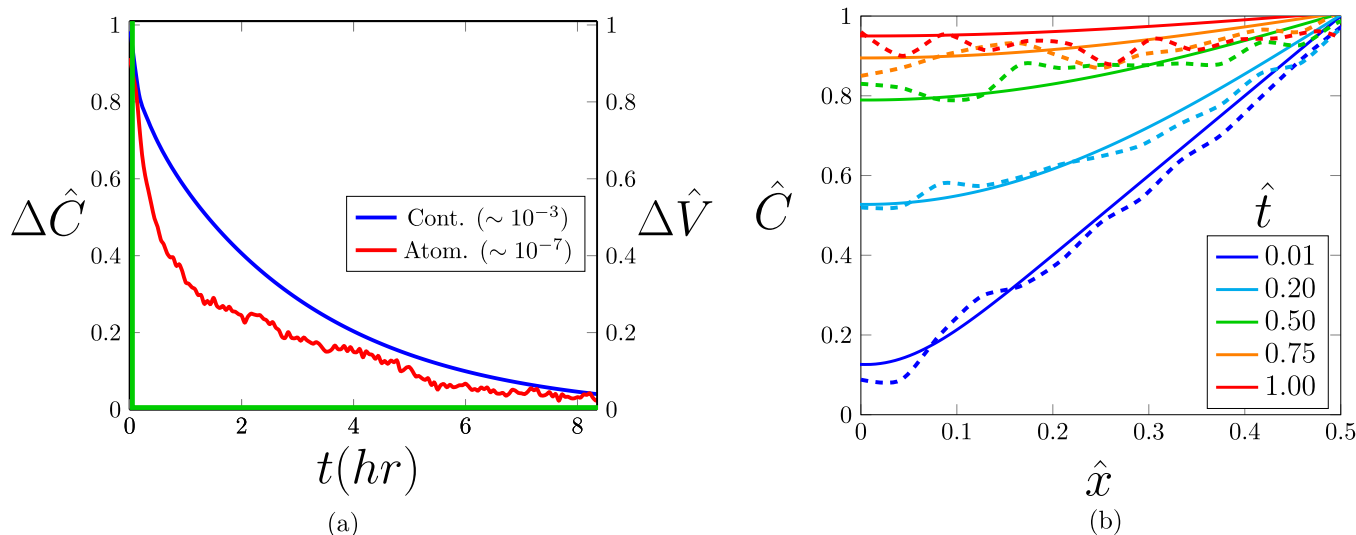
FIG. 11. Dynamics of the concentration gradient during relaxation in both scales. (a) The transient dynamics of the concentration gradient $\Delta\hat{C}$ during relaxation, in the continuum (blue) and in the equivalent simulation domain (red). (b) The profile of the relaxation of the concentration gradient in half-cell ($0 < \hat{x} < 0.5$) at various times, in both continuum (solid) and atomic (dotted) scales, before the convergence to the steady-state threshold.

TABLE V. Layers involved during formation/relaxation.

Medium	Formation/relaxation rate	Nature	Drive
Double layer	Fast	Electrical	Reaction
Boundary layer	Slow	Physical	Diffusion

scale of the SEI microstructure as ~20 − 70 nm,[84,85] its effect could be considered negligible.

In addition, while the smallest measured experimental branch and inter-branch scales [Figs. 9(c) and 9(d)] lie in the range of ~500 nm and ~100 nm, the typical scale for the equivalent atomistic simulation is ~Å, which means that the established simulation paradigm can project into a well below scale than the smallest possible experimental measurements. Such a mapping-down is important since most of the concentration and voltage drop occur in the very close vicinity of the branch surface (i.e., space charge region[31,86]), while the experimental observation falls short for zooming-in, below a certain scale.

Finally, the development of the smaller-scale equivalent framework (atomistic) for the larger scale event (continuum) in this work has been performed for a simplified electrochemical setup, which includes a domain of a certain scale l, the solution of a certain diffusivity D, and imposing a certain voltage V, and excludes additional effects such as the initial transition period and the role of microstructure, particularly on the diffusivity.

VI. CONCLUSIONS

Acknowledging the scale gap between the experiments and simulations, we have developed an electrochemically equivalent sim-

ulation paradigm of the smaller scale (~ nm) for an experiment of the larger scale (~ mm), in terms of dynamics of formation and relaxation of the ionic concentration. The new framework contains the equivalent length scale l_{EQ}, diffusivity D_{EQ}, and voltage V_{EQ}, where the underlying physics for obtaining each parameter has been established. The harmony of the dynamics between the experiments and simulations has been verified via time-matching of the formation and relaxation of the concentration profile in the sample computation. The results could be useful for projecting the dynamics of the prescribed experiments and particularly estimating the transition period to the steady-state regime of operation.

AUTHOR DECLARATIONS

Conflict of Interest

The authors have no conflicts to disclose.

Author Contributions

Asghar Aryanfar: Conceptualization (lead); Data curation (equal); Formal analysis (equal); Funding acquisition (equal); Investigation (equal); Writing – original draft (equal); Writing – review & editing (equal). **Trina Dhara**: Formal analysis (equal); Visualization (equal); Writing – original draft (equal); Writing – review & editing (equal). **Sunando DasGupta**: Funding acquisition (lead); Project adminis-

tration (equal). **William A. Goddard III**: Project administration (equal).

DATA AVAILABILITY

The raw data for producing the results in this manuscript are freely available upon request from the corresponding author at http://aryanfar@caltech.edu.

NOMENCLATURE

C_0	Bulk concentration ($mol\,m^{-3}$)
D_{EQ}	Equivalent diffusion coefficient (m^2s^{-1})
D_0	Diffusion coefficient (m^2s^{-1})
E	Electric field strength (Vm^{-1})
F	Faraday's constant ($Cmol^{-1}$)
i	Current density ($mA.\,cm^{-2}$)
k_B	Boltzmann's constant (JK^{-1})
l_{EQ}	Simulation domain length (nm)
l_0	Inter-electrode gap (mm)
V_{EQ}	Equivalent voltage (V)
V_0	Applied voltage (V)
x_I	Thickness of the space charge region (μm)
z	Valence of ions ([ ])
δ_p	Thickness of the inner diffusion layer (μm)
δ_s	Thickness of the outer diffusion layer (μm)
δt_{EQ}	Simulation time scale (s)
δt_0	Experimental time scale (s)
ε	Permittivity of solvent ([ ])
ε_0	Vacuum permittivity ($e^2eV^{-1}\mathring{A}^{-1}$)
λ_D	Debye length (nm)
μ	Ionic mobility ($m^2s^{-1}V^{-1}$)

REFERENCES

[1] J. Newman and N. P. Balsara, *Electrochemical Systems* (John Wiley & Sons, 2021).

[2] W. Giurlani, G. Zangari, F. Gambinossi, M. Passaponti, E. Salvietti, F. Di Benedetto, S. Caporali, and M. Innocenti, "Electroplating for decorative applications: Recent trends in research and development," Coatings **8**(8), 260 (2018).

[3] S. M. Oja, M. Wood, and B. Zhang, "Nanoscale electrochemistry," Anal. Chem. **85**(2), 473–486 (2013).

[4] K.-C. Pu, X. Zhang, X.-L. Qu, J.-J. Hu, H. W. Li, M.-X. Gao, H.-G. Pan, and Y.-F. Liu, "Recently developed strategies to restrain dendrite growth of Li metal anodes for rechargeable batteries," Rare Met. **39**(6), 616–635 (2020).

[5] W. Schwarzacher, "Electrodeposition: A technology for the future," Electrochem. Soc. Interface **15**(1), 32–33 (2006).

[6] M. Winter, B. Barnett, and K. Xu, "Before Li ion batteries," Chem. Rev. **118**(23), 11433–11456 (2018).

[7] F. Presuel-Moreno, M. A. Jakab, N. Tailleart, M. Goldman, and J. R. Scully, "Corrosion-resistant metallic coatings," Mater. Today **11**(10), 14–23 (2008).

[8] P. Nuss and M. J. Eckelman, "Life cycle assessment of metals: A scientific synthesis," PLoS One **9**(7), e101298 (2014).

[9] J. K. Jhothiraman and R. Balachandran, "Electroplating: Applications in the semiconductor industry," Adv. Chem. Eng. Sci. **9**(2), 239–261 (2019).

[10] H. Gerischer, "The impact of semiconductors on the concepts of electrochemistry," Electrochim. Acta **35**(11–12), 1677–1699 (1990).

[11] I. M. Dharmadasa and J. Haigh, "Strengths and advantages of electrodeposition as a semiconductor growth technique for applications in macroelectronic devices," J. Electrochem. Soc. **153**(1), G47 (2006).

[12] P. C. Andricacos, "Copper on-chip interconnections: A breakthrough in electrodeposition to make better chips," Electrochem. Soc. Interface **8**(1), 32 (1999).

[13] S. M. Merchant, S. H. Kang, M. Sanganeria, B. van Schravendijk, and T. Mountsier, "Copper interconnects for semiconductor devices," JOM **53**, 43–48 (2001).

[14] G. D. Wilcox, "Electrodeposition—A versatile tool for the surface engineer," Trans. IMF **85**(1), 8–13 (2007).

[15] Y. I. Supriyatna, R. Noviyana, E. G. Suka, B. N. Hidayah Kambuna, S. Sumardi, and Sudibyo, "Influence of current density in Cu-Mn electroplating of AISI 1020 steel corrosion rate," Mater. Today: Proc. **44**, 3289–3295 (2021).

[16] Y. Zhang, S. Zhang, Y. He, H. Li, T. He, Y. Fan, and H. Zhang, "Mechanical properties and corrosion resistance of pulse electrodeposited Ni-B/B_4C composite coatings," Surf. Coat. Technol. **421**, 127458 (2021).

[17] N. P. Wasekar, N. Hebalkar, A. Jyothirmayi, B. Lavakumar, M. Ramakrishna, and G. Sundararajan, "Influence of pulse parameters on the mechanical properties and electrochemical corrosion behavior of electrodeposited Ni-W alloy coatings with high tungsten content," Corros. Sci. **165**, 108409 (2020).

[18] Q. Yang, Q. Li, Z. Liu, D. Wang, Y. Guo, X. Li, Y. Tang, H. Li, B. Dong, and C. Zhi, "Dendrites in Zn-based batteries," Adv. Mater. **32**(48), 2001854 (2020).

[19] X. Zhang, A. Wang, X. Liu, and J. Luo, "Dendrites in lithium metal anodes: Suppression, regulation, and elimination," Acc. Chem. Res. **52**(11), 3223–3232 (2019).

[20] B. Lee, E. Paek, D. Mitlin, and S. W. Lee, "Sodium metal anodes: Emerging solutions to dendrite growth," Chem. Rev. **119**(8), 5416–5460 (2019).

[21] T. Dhara, U. U. Ghosh, A. Ghosh, B. S. Vishnugopi, P. P. Mukherjee, and S. DasGupta, "Mechanistic underpinnings of morphology transition in electrodeposition under the application of pulsatile potential," Langmuir **38**(16), 4879–4886 (2022).

[22] N. M. Schneider, J. H. Park, J. M. Grogan, D. A. Steingart, H. H. Bau, and F. M. Ross, "Nanoscale evolution of interface morphology during electrodeposition," Nat. Commun. **8**(1), 2174 (2017).

[23] N. D. Nikolić, K. I. Popov, Lj. J. Pavlović, and M. G. Pavlović, "Morphologies of copper deposits obtained by the electrodeposition at high overpotentials," Surf. Coat. Technol. **201**(3–4), 560–566 (2006).

[24] T. Dhara, A. Aryanfar, A. Ghosh, U. Ghosh, P. Mukherjee, and S. DasGupta, "The role of pulse duty cycle and frequency on dendritic compression," J. Phys. Chem. C **127**(9), 4407–4415 (2023).

[25] M. Li, L. Ran, and R. Knibbe, "Zn electrodeposition by an *in situ* electrochemical liquid phase transmission electron microscope," J. Phys. Chem. Lett. **12**(2), 913–918 (2021).

[26] W. Du, Z. Zhang, F. Iacoviello, S. Zhou, R. E. Owen, R. Jervis, D. J. L. Brett, and P. R. Shearing, "Observation of Zn dendrite growth via operando digital microscopy and time-lapse tomography," ACS Appl. Mater. Interfaces **15**(11), 14196–14205 (2023).

[27] N. Cheng, H. Sun, A. F. Beker, J. T. van Omme, E. Svensson, H. Arandiyan, H. R. Lee, B. Ge, S. Basak, R. A. Eichel *et al.*, "Nanoscale visualization of metallic electrodeposition in a well-controlled chemical environment," Nanotechnology **33**(44), 445702 (2022).

[28] A. Aryanfar, "Linearized tracking of dendritic evolution in rechargeable batteries," J. Electrochem. Soc. **169**(11), 112507 (2022).

[29] R. Akolkar, "Mathematical model of the dendritic growth during lithium electrodeposition," J. Power Sources **232**, 23–28 (2013).

[30] A. Aryanfar, M. R. Hoffmann, and W. A. Goddard III, "Finite-pulse waves for efficient suppression of evolving mesoscale dendrites in rechargeable batteries," Phys. Rev. E **100**(4), 042801 (2019).

[31] J. N. Chazalviel, "Electrochemical aspects of the generation of ramified metallic electrodeposits," Phys. Rev. A **42**(12), 7355–7367 (1990).

[32] M. Rosso, "Electrodeposition from a binary electrolyte: New developments and applications," Electrochim. Acta **53**(1), 250–256 (2007).

[33] C. Monroe and J. Newman, "Dendrite growth in lithium/polymer systems," J. Electrochem. Soc. **150**(10), A1377–A1384 (2003).

18 November 2024 17:54:51

[34]V. Fleury, J.-N. Chazalviel, M. Rosso, and B. Sapoval, "The role of the anions in the growth speed of fractal electrodeposits," J. Electroanal. Chem. Interfacial Electrochem. **290**(1–2), 249–255 (1990).

[35]V. Fleury, "Branched fractal patterns in non-equilibrium electrochemical deposition from oscillatory nucleation and growth," Nature **390**(6656), 145–148 (1997).

[36]R. Davidson, A. Verma, D. Santos, F. Hao, C. Fincher, S. Xiang, J. Van Buskirk, K. Xie, M. Pharr, P. P. Mukherjee, and S. Banerjee, "Formation of magnesium dendrites during electrodeposition," ACS Energy Lett. **4**(2), 375–376 (2018).

[37]T. Nishida, K. Nishikawa, M. Rosso, and Y. Fukunaka, "Optical observation of Li dendrite growth in ionic liquid," Electrochim. Acta **100**, 333–341 (2013).

[38]J. Steiger, D. Kramer, and R. Monig, "Mechanisms of dendritic growth investigated by in situ light microscopy during electrodeposition and dissolution of lithium," J. Power Sources **261**, 112–119 (2014).

[39]A. Aryanfar, D. Brooks, B. V. Merinov, W. A. Goddard III, A. J. Colussi, and M. R. Hoffmann, "Dynamics of lithium dendrite growth and inhibition: Pulse charging experiments and Monte Carlo calculations," J. Phys. Chem. Lett. **5**(10), 1721–1726 (2014).

[40]A. Aryanfar, S. Medlej, and W. A. Goddard III, "Morphometry of dendritic materials in rechargeable batteries," J. Power Sources **481**, 228914 (2021).

[41]F. Hao, A. Verma, and P. P. Mukherjee, "Mesoscale complexations in lithium electrodeposition," ACS Appl. Mater. interfaces **10**(31), 26320–26327 (2018).

[42]D. Tewari and P. P. Mukherjee, "Mechanistic understanding of electrochemical plating and stripping of metal electrodes," J. Mater. Chem. A **7**(9), 4668–4688 (2019).

[43]B. Ghalami Choobar, H. Modarress, R. Halladj, and S. Amjad-Iranagh, "Electrodeposition of lithium metal on lithium anode surface, a simulation study by: Kinetic Monte Carlo-embedded atom method," Comput. Mater. Sci. **192**, 110343 (2021).

[44]L. A. Selis and J. M. Seminario, "Dendrite formation in Li-metal anodes: An atomistic molecular dynamics study," RSC Adv. **9**(48), 27835–27848 (2019).

[45]Y. Hiwatari, Y. Kaneko, T. Mikami, K. Ohara, and F. Asa, "Molecular dynamics—Monte Carlo hybrid simulation of thin film growth and void formation in electrodeposition process," Mol. Simul. **33**(1–2), 133–138 (2007).

[46]M. Feng, C.-T. Yang, and Y. Qi, "The critical stack pressure to alter void generation at Li/solid-electrolyte interfaces during stripping," J. Electrochem. Soc. **169**(9), 090526 (2022).

[47]C.-T. Yang and Y. Qi, "Maintaining a flat Li surface during the Li stripping process via interface design," Chem. Mater. **33**(8), 2814–2823 (2021).

[48]B. S. Vishnugopi, F. Hao, A. Verma, and P. P. Mukherjee, "Double-edged effect of temperature on lithium dendrites," ACS Appl. Mater. Interfaces **12**(21), 23931–23938 (2020).

[49]B. S. Vishnugopi, M. B. Dixit, F. Hao, B. Shyam, J. B. Cook, K. B. Hatzell, and P. P. Mukherjee, "Mesoscale interrogation reveals mechanistic origins of lithium filaments along grain boundaries in inorganic solid electrolytes," Adv. Energy Mater. **12**(3), 2102825 (2022).

[50]D. C. Grahame, "The electrical double layer and the theory of electrocapillarity," Chem. Rev.s **41**(3), 441–501 (1947).

[51]M. Nakamura, N. Sato, N. Hoshi, and O. Sakata, "Outer Helmholtz plane of the electrical double layer formed at the solid electrode–liquid interface," ChemPhysChem **12**(8), 1430–1434 (2011).

[52]M. Z. Bazant, K. Thornton, and A. Ajdari, "Diffuse-charge dynamics in electrochemical systems," Phys. Rev. E **70**(2), 021506 (2004).

[53]N. Ibl, "Some theoretical aspects of pulse electrolysis," Surf. Technol. **10**(2), 81–104 (1980).

[54]A. Namisnyk and J. Zhu, "A survey of electrochemical super-capacitor technology," in Australian Universities Power Engineering Conference (University of Canterbury, New Zealand, 2003).

[55]J. Lyklema, Fundamentals of Interface and Colloid Science: Particulate Colloids (Elsevier, 2005).

[56]J. O'M. Bockris, A. K. N. Reddy, and M. E. Gamboa-Adelco, Modern Electrochemistry 1, 2A, and 2B (Springer, 2006).

[57]N. Ibl, J. C. Puippe, and H. Angerer, "Electrocrystallization in pulse electrolysis," Surf. Technol. **6**(4), 287–300 (1978).

[58]P. Jean, "One and a half century of diffusion: Fick, Einstein, before and beyond," Diffus. Fundam. **4**(6), 1–19 (2006).

[59]D. B. Hibbert and J. R. Melrose, "Electrodeposition in support: Concentration gradients, an ohmic model and the genesis of branching fractals," Fractals Nat. Appl. Sci. **423**(1864), 149–158 (1990).

[60]T. J. Collins, "ImageJ for microscopy," Biotechniques **43**(sup1), S25–S30 (2007).

[61]R. Kumar, T. Dhara, H. Hu, and M. Chakraborty, "Visualization-based prediction of dendritic copper growth in electrochemical cells using convolutional long short-term memory," Energy AI **10**, 100203 (2022).

[62]P. M. Iannaccone and M. Khokha, Fractal Geometry in Biological Systems: An Analytical Approach (CRC Press, 1996).

[63]T. Vicsek, Fractal Growth Phenomena (World Scientific, 1992).

[64]A. Y. Cherny, E. M. Anitas, V. A. Osipov, and A. I. Kuklin, "Small-angle scattering from the Cantor surface fractal on the plane and the Koch snowflake," Phys. Chem. Chem. Phys. **19**(3), 2261–2268 (2017).

[65]G. B. So, H.-R. So, and G.-G. Jin, "Enhancement of the box-counting algorithm for fractal dimension estimation," Pattern Recognit. Lett. **98**, 53–58 (2017).

[66]J. Feng, W.-C. Lin, and C.-T. Chen, "Fractional box-counting approach to fractal dimension estimation," in Proceedings of the 13th International Conference on Pattern Recognition (IEEE, 1996), Vol. 2, pp. 854–858.

[67]K. Falconer, Fractal Geometry: Mathematical Foundations and Applications (John Wiley & Sons, 2007).

[68]P. Gębara, M. Gębara, and A. Owczarek, "Fractal structures in electrodeposition process," Acta Phys. Pol., A **138**(2), 287–290 (2020).

[69]J. Li, Q. Du, and C. Sun, "An improved box-counting method for image fractal dimension estimation," Pattern Recognit. **42**(11), 2460–2469 (2009).

[70]A. Zhokh, A. Trypolskyi, and P. Strizhak, "Relationship between the anomalous diffusion and the fractal dimension of the environment," Chem. Phys. **503**, 71–76 (2018).

[71]M. C. Shelberg, N. Lam, and H. Moellering, "Measuring the fractal dimensions of surfaces," DTIC Report No. ADA129664 (1983).

[72]R. A. Noulty and D. G. Leaist, "Diffusion in aqueous copper sulfate and copper sulfate-sulfuric acid solutions," J. Solution Chem. **16**(10), 813–825 (1987).

[73]J. Newman and K. E. Thomas-Alyea, Electrochemical Systems (John Wiley & Sons, 2012).

[74]C. Brissot, M. Rosso, J. N. Chazalviel, and S. Lascaud, "Concentration measurements in lithium/polymer-electrolyte/lithium cells during cycling," J. Power Sources **94**(2), 212–218 (2001).

[75]E. Isaacson and H. B. Keller, Analysis of Numerical Methods (Courier Corporation, 1994).

[76]J. Crank and P. Nicolson, "A practical method for numerical evaluation of solutions of partial differential equations of the heat-conduction type," Math. Proc. Cambridge Philos. Soc. **43**, 50–67 (1947).

[77]National Institute of Standards and Technology, The NIST Reference on Constants, Units and Uncertainty (National Institute of Standards and Technology, NIST Physics Laboratory, 1998).

[78]E. A. Gomaa and R. T. Rashad, "Thermodynamic parameters for solvation of copper sulfate in (ethanol-water) mixed solvent at different temperatures," Asian J. Nanosci. Mater. **1**(2), 81–89 (2018).

[79]A. Lanjan, Z. Moradi, and S. Srinivasan, "Multiscale investigation of the diffusion mechanism within the solid–electrolyte interface layer: Coupling quantum mechanics, molecular dynamics, and macroscale mathematical modeling," ACS Appl. Mater. Interfaces **13**(35), 42220–42229 (2021).

[80]S. J. An, J. Li, C. Daniel, D. Mohanty, S. Nagpure, and D. L. Wood III, "The state of understanding of the lithium-ion-battery graphite solid electrolyte interphase (SEI) and its relationship to formation cycling," Carbon **105**, 52–76 (2016).

[81]H. Adenusi, G. A. Chass, S. Passerini, K. V. Tian, and G. Chen, "Lithium batteries and the solid electrolyte interphase (SEI)—Progress and outlook," Adv. Energy Mater. **13**(10), 2203307 (2023).

[82]D. Aurbach, M. L. Daroux, P. W. Faguy, and E. Yeager, "Identification of surface films formed on lithium in propylene carbonate solutions," J. Electrochem. Soc. **134**(7), 1611 (1987).

18 November 2024 17:54:51

[83] P. Keil, D. Lützenkirchen-Hecht, and R. Frahm, "Investigation of room temperature oxidation of cu in air by yoneda-xafs," AIP Conf. Proc. **882**, 490–492 (2007).

[84] X.-B. Cheng, R. Zhang, C.-Z. Zhao, F. Wei, J.-G. Zhang, and Q. Zhang, "A review of solid electrolyte interphases on lithium metal anode," Adv. Sci. **3**(3), 1500213 (2016).

[85] G. Yasin, M. Arif, T. Mehtab, X. Lu, D. Yu, N. Muhammad, M. T. Nazir, and H. Song, "Understanding and suppression strategies toward stable Li metal anode for safe lithium batteries," Energy Storage Mater. **25**, 644–678 (2020).

[86] C. Brissot, M. Rosso, J. N. Chazalviel, and S. Lascaud, "In situ concentration cartography in the neighborhood of dendrites growing in lithium/polymer-electrolyte/lithium cells," J. Electrochem. Soc. **146**(12), 4393–4400 (1999).

18 November 2024 17:54:51